Article:
Song, B., Li, Y., Wei, J. et al. (4 more authors) (2025) Enhancing the impact performance of TaNbHfZr high-entropy alloy film by interface strengthening and stress dispersion: Microstructure and mechanism. Materials Today Communications, 44. 112127. ISSN 2352-4928

https://doi.org/10.1016/j.mtcomm.2025.112127

Enhancing the impact performance of TaNbHfZr high-entropy alloy film by interface strengthening and stress dispersion: Microstructure and mechanism

Baorui Song[a, b], Yanhuai Li[c], Jiahong Wei[a, b], Dan Qian[c], Liuquan Yang[d], Zhongxiao Song[c], Weihua Li[a, b, e, *]

[a] Henan Academy of Sciences, Zhengzhou 450046, Henan, P.R. China

[b] Institute of Chemistry, Henan Academy of Sciences, Zhengzhou 450046, Henan, P.R. China

[c] State Key Laboratory for Mechanical Behavior of Materials, Xi'an Jiaotong University, Xi'an 710049, Shaanxi, P.R. China

[d] Institute of Functional Surfaces, School of Mechanical Engineering, University of Leeds, Leeds LS2 9JT, United Kingdom

[e] North China University of Water Resources and Electric Power, Zhengzhou 450046, Henan, P.R. China

* Authors to whom correspondence should be addressed.

Email:

Weihua Li: liweihua1928@163.com

Keywords: High-entropy Alloy Film; TaNbHfZr; Sandwich-structure; Nano-impact; Microstructure; Mechanism

Abstract

The sandwich-structured TaNbHfZr refractory high-entropy alloy film (RHEAF) was fabricated by magnetron sputtering. Nano-impact was utilized to extract the local mechanical response of the film with severe localized strain due to the high instantaneous strain rate (*ISR*). Analysis on dynamic hardness (H_D) and toughness of TaNbHfZr film was carried out quantitatively. The plasticity absorption ability in nano-impact is higher indicated by the increased plastic work (W_p) with increasing acceleration

force (*AF*). The decreased H_D is attributed to the contribution of the energy to the fracture at higher *AF*. Through TEM observation, the dynamic response is confirmed by thickness reduction in nano-impact. Cracks occur where the stress reaches its maximum in the middle layer, near the middle-bottom boundary, serving as the primary energy-storage mechanism in the sandwich-structured TaNbHfZr film. Furthermore, the rate-controlling response can be attributed to the dislocation motion at varing loading rates. This phenomenon is confirmed by FEM simulation. Here, the equiaxed grains within the middle layer mitigate further catastrophic damage by absorbing the localized and concentrated stress through rotation or grain boundary sliding. Consequently, the film was strengthened and stabilized due to the effective stress dispersion and existence of interface in the sandwich structure.

1 Introduction

High-entropy alloys (HEAs), as a fundamentally new alloying concept, has been firstly proposed by Yeh *et al.* [1] in 2004. HEAs have high configurational entropies at a random state (≥1.5*R*, *R* is the ideal gas constant), which can stabilize the simple crystal structure by forming solid solutions such as fcc (face-centered cubic) and bcc (body-centered cubic) solid-solution structures, rather than complex intermetallic phases [2]. The high-entropy and severe lattice distortion effects lead to a rugged energy landscape which increases the resistance to dislocation motion and pronounced solid solution strengthening for HEAs [3, 4]. Compared with traditional refractory metals and alloys, HEAs pave a new way for an excellent combination of superior functional properties, which have great potential for practical applications. HEAs composed of high melting-point elements such as Cr, Hf, Mo, Nb, Ta, W, Zr *etc.* named refractory high-entropy alloys (RHEAs), exhibiting outstanding strength and exceptional oxidation resistance [5, 6]. The reported RHEAs with bcc structure such as

WNbMoTa, WNbMoTaV [5], $Hf_{25}Nb_{25}Ti_{25}Zr_{25}$ [7], $HfMo_xNbTaTiZr$ [8] possess superior mechanical performance. Feng *et al.* [9] have prepared NbMoTaW films via magnetron sputtering and reported its superior nanoindentation hardness (~16 GPa) due to the source strengthening and solid solution hardening mechanisms using a thermally activated dislocation model.

The mechanism of plastic deformation is usually recognized to be rate-dependent. Definitely speaking, quasi-static and dynamic high strain rate conditions fall into the strain rate range of 10^{-5}~10^{-1} s^{-1} and $>5\times10^{1}$ s^{-1}, respectively [10]. The dynamic performance of the HEAFs is often involved in practical applications such as high-speed transportation vehicles and hydraulic machinery *etc.* [11]. Nano-impact makes it possible to quantify energy absorption of a material surface in nano-/micro-scale and provides valuable highly localized information about deformation acting as an effective measurement of impact energy to determine the fracture resistance [12].

As evidenced by Gray and Hirsch *et al*. [13, 14], the dislocation structures are substantially different between low strain rate and high strain rate via TEM (transmission electron microscopy) micrographs. The rate-dependence for bcc metals suggests that the deformation occurs via thermally activated kink-pair nucleation which is a typical screw dislocation propagation mechanism [15]. Twining and shear bands related deformation mechanisms are proposed at lower strain rates and softening even occurs at higher strain rates. Nemat-Nasser *et al.* [16] reported that phenomena like shear bands, dynamic recovery, dislocation lines, dislocation forests and deformation dislocation loops arise in the dynamic deformation with strain rate $>5\times10^{4}$ s^{-1} for bcc Ta, as well as slip of the perfect screw dislocations on {110}-type primary planes as the dominant deformation mechanism, which are confirmed via TEM analysis. The yield

strength of as-cast TiHfZrTaNb HEA at the initial strain rates ~3.4×10^{3} s^{-1} with localized in macroscopic shear bands was about ~40 % higher than that measured at ~10^{-3} s^{-1} with evenly distributed shear bands by compression due to the increase of the dislocation density [17]. The dynamic fracture often emerges as one type of the phenomena during the overall process of a target impacted by a projectile [18]. While for nanocrystalline and ultrafine bcc V, shear banding rather than crack initiation and propagation is observed with promoting shear localization in dynamic compression with strain rate of ~10^{3} s^{-1} [19].

However, RHEAs always exhibit apparent brittleness and lack of room-temperature ductility, which remains major and important challenges for their processing and application [20]. Combining the ductile material with the hard one to coordinate the comprehensive excellent performance of RHEAs is meaningful and necessary. Zhao *et al.* [21] prepared a Cu/(NbMoTaW) nanolaminates introducing the hard NbMoTaW HEA laminates into the soft Cu to form the ultra-strong Cu/HEA composites. Besides, as reported by Wei *et al.* [20], the TiVNbHf RHEA gets more ductile with higher fracture elongation due to the evolution to fully equiaxed grain after homogenization. Herein, we developed a body-centered cubic (bcc) sandwich-structured TaNbHfZr film. This designed film integrates exceptional ductility of the middle layer characterized by equiaxed grains, with enhanced resistance to softening in the upper and lower layers which feature columnar grains. We evaluated the mechanical behavior of magnetron-sputtered TaNbHfZr RHEAF in terms of the high strain rate hardness H_D by nano-impact and also bridge the correlation of the plasticity and toughness under test conditions with different strain rates. At the same time, we introduce the energy-related evaluation to discuss the plasticity evolution during the dynamic impact deformation as well as the corresponding mechanisms.

2 Materials and Methods

2.1 Film deposition and characterization

The TaNbHfZr target (φ75 × 5 mm) was prepared via powder metallurgy with purities higher than 99.99% and was nominally equiatomic ($Ta_{25}Nb_{25}Hf_{25}Zr_{25}$). The (100) Si wafer substrates were cleaned ultrasonically in acetone, absolute ethyl alcohol and deionized water sequentially before deposition. The base pressure of the vacuum system during deposition via magnetron sputtering (JPG450a dual-chamber magnetron sputtering deposition system) was less than 1×10^{-4} Pa. The deposition process was conducted by DC source in an argon atmosphere with a target power of 200 W. The Ar flow rate was maintained at 25 sccm, and the working pressure was 0.4 Pa. The substrate bias was set at -100 V with substrate heating to 700 °C before the deposition. To achieve the layered structure, the film was initially deposited at 700 °C for 18 mins, marked as stage 1; followed by a 12-minute interruption of the heating process, marked as stage 2. Subsequently, the heater was reactivated for an additional 30 mins, marked as stage 3. During the whole process, the entire deposition was continuous, with only the substrate temperature being changed, and the total deposition time was 60 mins. The finer columnar grains in the lower layer were obtained at stage 1, the equiaxed grains in the middle layer were obtained at stage 2, and the coarser columnar grains in the upper layer were obtained at stage 3.

The phase structure of the TaNbHfZr film was characterized with Cu Kα radiation on a Bruker D8 discover powder X-Ray diffractometer at room temperature, at a scan speed of 2°/min from 10°-120°. Scanning electron microscopy (SEM, FEI-VERIOS460) was employed to observe the surface morphologies. High-resolution transmission electron microscopy (HR-TEM, JEM-2100F) experiment was conducted to observe and determine the

cross-sectional microstructure of the TaNbHfZr film, as well as the elemental composition via energy dispersive X-Ray spectroscopy (EDS) analysis. The atomic force microscope (AFM, INNOVA) was used to analyze the surface roughness of these films.

The TEM foil for deformed specimen of nanoindentation at load=50 mN with *LR*=0.5 mN/s and nano-impact at *AF*=5 mN were prepared using the Helios G4 CX FIB (Focused Ion Beam) workstation. 30 KeV was used to lift out the cross-section sample from one corner to the opposite side of the indentation imprint. The coarse and fine milling was performed at the current from 0.79 nA, 0.43 nA, 0.23 nA to 80 pA. Low-energy cleaning was then performed at 5 KeV and 2 KeV after the milling. The TaNbHfZr pillars were prepared using FIB with diameter of 400 nm and height/diameter ratio of 2.5.

2.2 Nanomechanical tests

The nano-impact and nanoindentation experiments were carried out in a controlled environment (25 °C and 65% relative humidity) using a NanoTest Vantage system (Micro Materials Ltd, Wrexham, UK). A calibrated diamond Berkovich indenter with a nominal tip curvature radius of ~50 nm was utilized for nano-impact and nanoindentation tests. The area function of the indenter was calibrated based on measurements from a fused silica reference sample. The apparatus of nano-impact is illustrated in **Figure 1**. For the nano-impact test, the *AF* was set at 5, 15 and 30 mN. The indenter was positioned at an accelerated distance (*AD*) of 15 μm from the sample. The loading coil current was maintained constant throughout the impact. As a result, the kinetic energy (*KE*) of the pendulum increased until contact occurred, and the indenter reached its maximum penetration depth in the sample before rebounding. The indenter ultimately settled on the surface after several “bounces”. The plastic deformation was completed in the first cycle, rendering the

influence of subsequent rebounds on the final impression depth insignificant [22]. The effective pendulum mass was 210 g. Owing to the flat and smooth surface of the TaNbHfZr film, each nano-impact at an *AF* was repeated 3 times with a 50 μm interval. The residual contact area of the nano-impact at *AF*=5, 15 mN was measured using Image-J software.

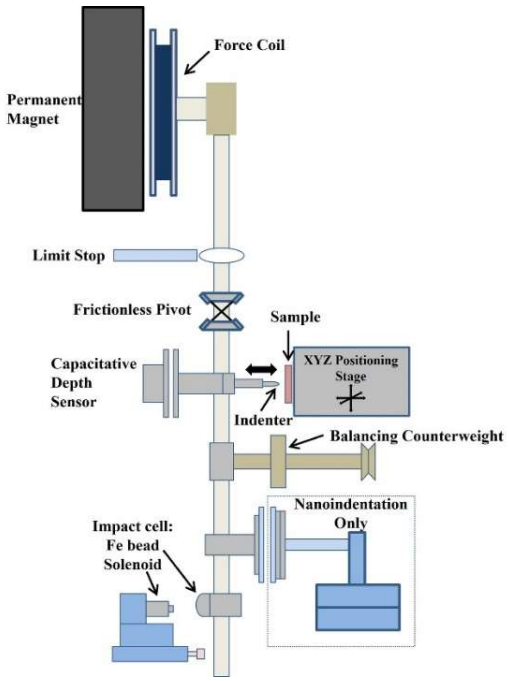

Figure 1 Schematic diagram of experimental apparatus used to quantify the impact response (referred and modified from ref. [13])

2.3 FEM modeling of cracking

The mechanical model was constructed in a 2D axisymmetric framework, simulating a plane-strain state. The system employed a four-node bilinear plane strain quadrilateral element (CPE4R) governed by reduced integration and hourglass control. During the indentation process, the mesh was refined to a size of 50 nm. The indenter was conceptualized as analytical rigid body, and its conico-spherical profile was designed to fit the area shape function $A(h)$ of a Berkovich indenter (where $A(h)$ is the indenter section at a distance h from the tip apex). The opening angle of

the indenter was 70.32°. The simulation cell was taken sufficiently wide to prevent the stress/strain fields generated within the sample during indentation from interacting with the outer boundary. Additionally, a 5 μm thickness for the silicon substrate within the computational cell was deemed adequate. The crack propagation was implemented using a coupled Cohesive Zone Model (CZM), and the crack openings followed the cohesive traction-separation law [23]. In this instance, the maximum principal stress criterion was selected for crack initiation. For the constructed model, the set of simultaneous non-linear dynamic equilibrium equations were solved iteratively using Newton's method.

3 Results and discussion

3.1 Microstructural analysis

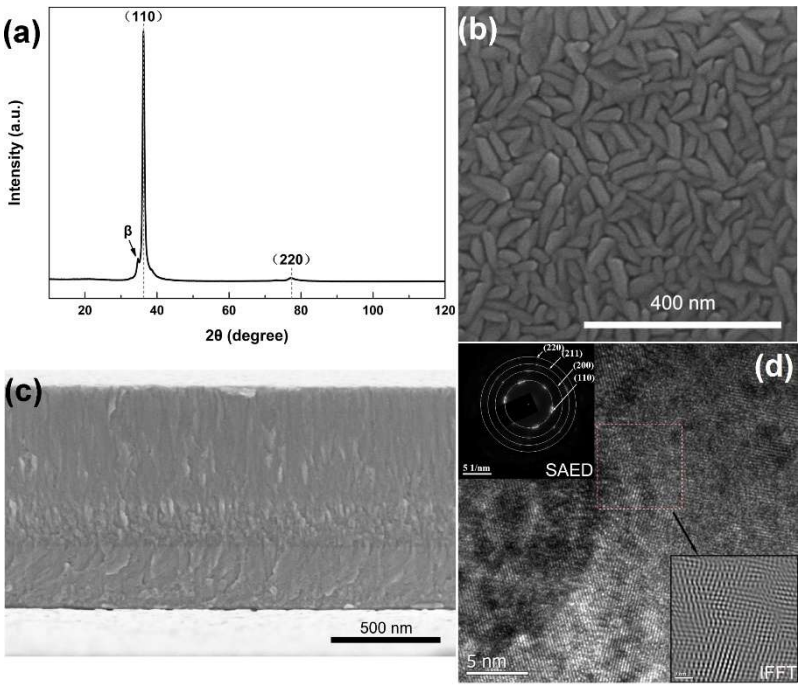

Figure 2 (a) XRD pattern; SEM image of **(b)** surface morphology; **(c)** cross-sectional morphology; **(d)** HR-TEM image, inserts are the SAED (Selected Area Electron Diffraction) and the IFFT (Inverse Fast Fourier Transformation) images of the selected area denoted by a red dotted

square for the as-deposited TaNbHfZr film.

The XRD pattern of the as-deposited TaNbHfZr film, depicted in **Figure 2 (a)**, reveals that the primary phase structure is body-centred (bcc), characterized by a dominant (110) plane at ~37°. Additionally, a minor secondary β hcp phase is present at ~35°, as indicated in previous work [24, 25]. In **Figure 2 (b)**, the top surface is characterized by needle-like granules with width ranging from 30 to 40 nm. At high deposition temperature, the coarsening driving force through surface atomic diffusion and grain boundary movement enhances, thus the particles on the film surface coalesce along preferred orientation as needle shape to reduce the total surface energy and interface energy [9, 26]. Additionally, the surface is densely packed and devoid of any hole. AFM analysis in **Figure S1** shows the surface average roughness R_a is ~2 nm. The cross-sectional morphology in **Figure 2 (c)** depicts the dense morphology and a sandwich layered structure with a total thickness of 1 μm (300 nm for lower columnar-grain layer, 200 nm for equiaxed-grain middle layer and 500 nm for upper columnar-grain layer). In addition, there is a good adhesion between columnar and equiaxed grain structures, characterized by clear and intact interfaces. The EDS analysis indicates that the film possesses nearly equiatomic elemental compositions of Ta, Zr, Nb, Hf (25 at. %, 24 at. %, 29 at. % and 22 at. %, respectively). The HR-TEM analysis in **Figure 2 (d)** exhibits clear and continuous lattice fringes in both the HR-TEM and IFFT images. Besides, some lattice distortion can be discerned due to atomic-size mismatch and elastic-modulus mismatch within the average bcc lattice [27].

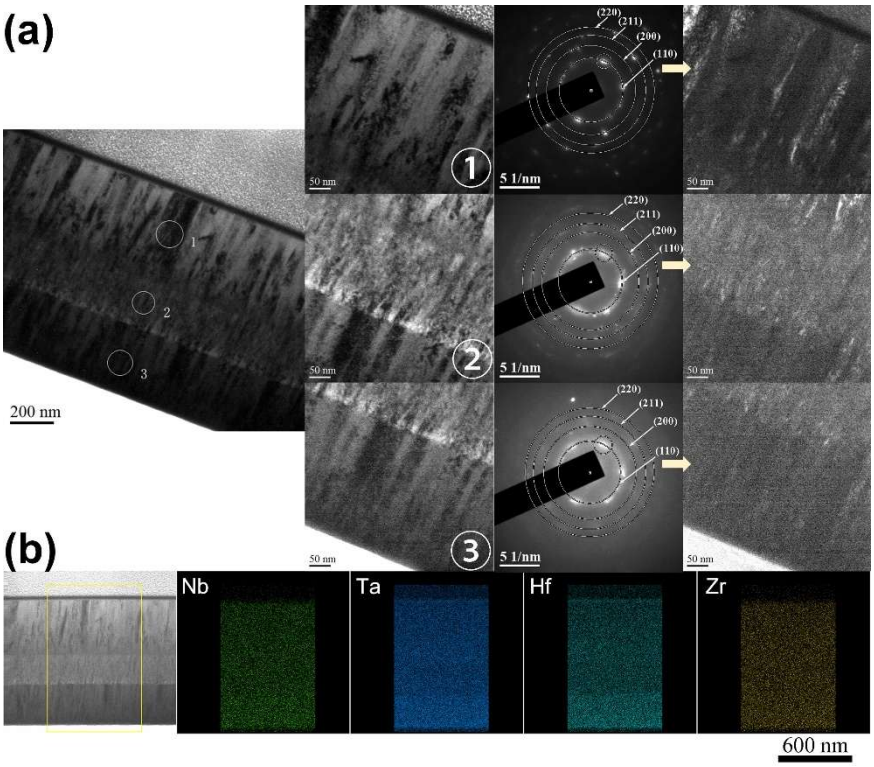

Figure 3 (a) SAED and corresponding DF (dark field) images of different layers; **(b)** EDS-mapping of elemental distribution for as-deposited TaNbHfZr film.

TEM analysis of the as-deposited TaNbHfZr film lifted out by FIB is shown in **Figure 3 (a)**. The distinct layered structure is characterized by elongated and coarser columnar grains extending throughout the upper layer, equiaxed grains with sizes differ little in all directions in the middle layer, and finer columnar grains in the bottom layer can be seen. SEAD images help to characterize each layer with clearly separated spots in the top layer, fine and continuous spots in the middle layer, and coarser spots compared with those in the top layer. DF images on the right specifically present the shape and size of the grains in each layer (the light part indicates the grains circled in SAED). The elemental distribution of each layer was homogeneous as demonstrated in **Figure 3 (b)**. The phase structure of three layers were identical, all keeping BCC structure with crystal plane of (110), (200), (211) and (220). At stage 1, the deposition

temperature (T_s) is 700 °C, and the melting point (T_m) of TaNbHfZr is 2385.8 °C, T_s / T_m=0.3. In this zone, the film is more prone to form refined grains with a certain texture, thus finer columnar grains formed [26]. At stage 2, the cooling effect during the temperature break-off bringing increased nucleation points and nucleation points, with the high-entropy and sluggish diffusion effects, as well as the heavy transition elements composed in the film, lead to variations in diffusion velocity of atoms during deposition. This favors the formation of refined equiaxed grains in the middle layer of the film, due to increased compositional undercooling [28, 29]. Besides, at lower deposition temperature, the ability of atoms to migrate decreases, resulting in limited surface diffusion, increased nucleation points and nucleation density, as well as decreased driving force for recrystallization, which contributes to the formation of equiaxed grains [30]. During the continuous deposition process, compared to stage 1, stage 3 no longer needs to form nucleation sites through the diffusion and rearrangement of atoms. At stage 3, a large number of nucleation sites undergo significant growth and recrystallization, giving rise to the formation of numerous coarser columnar grains in the upper layer of the film.

3.2 Nano-impact

3.2.1 Analysis of real-time impact depth curves

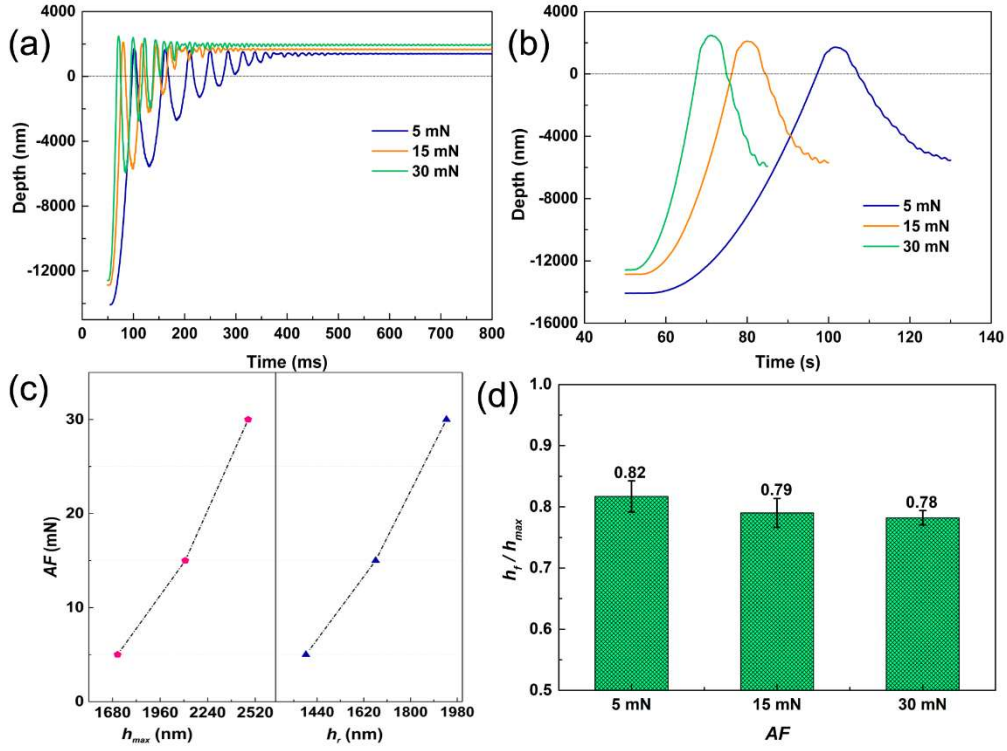

Figure 4 (a) Typical real time-depth curves; **(b)** the 1st cycle depth-time curves; **(c)** h_{max}, h_r vs. *AF* curves; **(d)** h_r/h_{max} of TaNbHfZr HEAFs for nano-impact at *AF*=5, 15, 30 mN.

The typical real-time depth curves of nano-impact at *AF*=5, 15 and 30 mN are shown in **Figure 4 (a)**, where the apparent oscillation can be seen due to the dynamic compliance of the pendulum during the reciprocal loading of impact. Some error may be introduced to the measurement of the rebound energy and lengthening the period at the maximum depth during impact [31]. The deep impact depth indicates strong dynamic response of the film during impact. However, considering that most permanent deformation has been completed in the 1st contact cycle, the detailed energy dissipation in this cycle was examined. The contact cycle consists of four phases as depicted in **Figure S2 (a)**: acceleration, indentation, rebound and deceleration. As supposed, higher *AF* corresponds to the higher h_{max} and h_r in **Figure 4 (c)**. Toughness is the ability of a material to

absorb energy during deformation up to fracture, while fracture toughness is the ability to resist the growth of a preexisting crack [32]. We use toughness here to encompass both the energy required to crack and to enable the crack to propagate until fracture, including the cases from lower to higher *AF*. The calculated h_r/h_{max} value illustrated in **Figure 4 (d)** is used as the index to measure the toughness [33], where h_r denotes the plastic deformation during the impact process. The results exhibit that the h_r/h_{max} decreased from 0.82 to 0.78 as *AF* increases in nano-impact, suggesting an increase in plasticity absorption.

3.2.2 SEM morphologies for the impact imprints and microcompression pillar

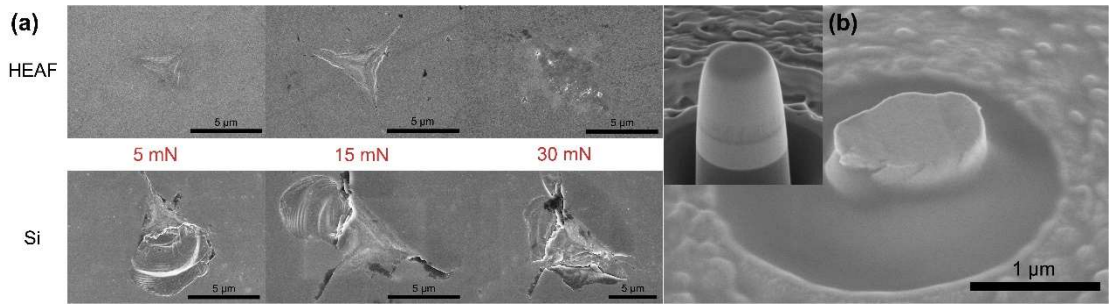

Figure 5 (a) SEM morphologies of impact imprints for TaNbHfZr HEAF and Si substrate at *AF*=5, 15, 30 mN; **(b)** the morphology of the pillar at loading rate of 1 nm/s before (inset) and after compression.

The SEM morphologies of the impact imprints of TaNbHfZr film and Si substrate are displayed in **Figure 5 (a)**. At *AF*=30 mN, the TaNbHfZr film delaminated from the Si substrate, leaving a shallow imprint. In contrast, uncoated Si exhibited visible radial cracks even at 5 mN, indicating that the deleterious effect becomes more pronounced at higher *AF*. Obviously, the protective film prevents the substrate from further degradation. The emergence of cracks reveals that the film requires increased ductility to resist cracking, fracture or spallation under dynamic impact. It has been confirmed that thinner film experiences higher stresses at the film-

substrate interface [27, 34]. Failure mechanisms during impact can be attributed to: micro-cracks initiation in the film post-impact; continued nucleation, coalescence, or propagation of cracks at the film-substrate interface, as indicated by minimal depth change in early impact cycles; debonding at the interface due to interfacial mismatch during plastic deformation and relaxation of pre-existing residual stress in the film [31, 35]. Microcracks form at the contact edge due to peak stress [33], which can also been verified by the following FEM sumulation results. Rupture behavior near the film-substrate interface, observed in quasi-static micro-compression tests at loading rates of 1 nm/s in **Figure 5 (b)** and 5 nm/s in **Figure S3**, provides evidence of fracture phenomenon consistent with the aforementioned failure mechanisms. The measured nanoindentation hardness at 50 mN of Si substrate is ~11.7±0.19 GPa, and the reduced modulus is ~177.1±1.55 GPa. For this harder film / softer substrate system, a larger deformation of the Si substrate will occur during impact when the penetration depth of the indenter reaches or deeper than the film/substrate interface. Besides, the deformation of Si substrate can cause the film to bend or peel off, aggravating the dynamic effect in nano-impact.

3.2.3 Dynamic hardness

We use the Meyer hardness as a representation of H_D [36]

$$H_D = \frac{P_m}{A} \qquad \textbf{Equation 1}$$

For a self-similar indenter geometry, A_c can be measured from microscopic observations of the impact impression, P_m represents the maximum resistance force obtained at the maximum depth of contact during impact, which is entirely determined by the dynamic compliance of the instrument, the sample properties and the geometry and initial impact energy of the indenter [37]. The proposed model, which includes the motion of the pendulum and the additional resistance accompanying the

indenter once contact begins and increases, can be expressed mathematically as [22, 38]

$$m\vec{a} + c\vec{v} + k\vec{x} + \overrightarrow{F(x)} = \overrightarrow{AF} \qquad \textbf{Equation 2}$$

where *c* represents the damping coefficient, primarily due to air damping. k signifies the spring stiffness, $\vec{x}$ is the indentation depth vector, and *a* is the acceleration velocity, which can be derived from the second derivative of the fitted *h-t* curve during the indentation phase in 1st cycle impact using the 5th-order polynomial fitting. As the plastic deformation was completed at the initial contact, we analyzed the first cycle of impact at *AF*=5 mN qualitatively. When the penetration depth approaches its maximum, damping effects are considerably reduced, and hence, the resistive force *F*(*x*) can be approximated as

$$F(x) = P_m \approx ma + AF \qquad \textbf{Equation 3}$$

The method to obtain *a* and P_m is illustrated in **Figure S2. (b)**. The theoretical H_D can be derived using **Equation 1-3**, with the results summarized in **Table 1**. Based on the one-dimensional model proposed by Andrews and Constantinides *et al.* [38, 39], the H_D of aluminum 1100 measured by nano-impact was slightly higher than its static hardness. While the dynamic hardness experiences obvious reduction when fracture occurs. The contribution of the energy transfers from plastic deformation to crack or fracture so that the resistance for the plastic deformation weakens and correspondingly the hardness decreases sharply. The calculated H_D is higher at *AF*=5 mN with 8.57 GPa to 7.09 GPa at *AF*=15 mN in dynamic nano-impact without considering the energy dissipation in cracks and fracture. This can be explained by the strain gradient plasticity (*SGP*) theory that dislocation density increases at decreased loads caused by the presence of *GND* [22, 40, 41].

Table 1 The calculated result of nano-impact at *AF*=5, 15 mN.

***AF* (mN)**	**H_D (GPa)**	**W_P (nJ)**	**△*E* (nJ)**	**U_{fra} (nJ)**
5	8.57	18.80	22.79	3.99
15	7.09	40.38	87.11	46.72

3.2.4 Impact energy

The energy loss during acceleration is estimated to be approximately 44.7 % due to energy dissipation in the system from damping and friction [35, 37]. The effective acceleration transfer work increases with *AF* [42]. For simplicity, we have omitted the thermal energy and damping effect induced energy loss. As shown in **Table 1**, the contribution to the fracture part also increases from 3.99 nJ of 5 mN to 46.72 nJ of 15 mN, exhibiting the apparent rate-dependent behavior. The kinetic energy difference (△*E*) can be equivalently considered as the sum of the (W_P) and fracture work (U_{fra}). Specifically, it is assumed that all the fracture work is absorbed by the film only. W_P is calculated using Tabor's method [36]. To determine U_{fra}, we introduce the following relationship

$$U_{fra}=0.553\Delta E - W_P = 0.2765\mathrm{m}({v_{in}}^2 - {v_{out}}^2) - \frac{1}{3}A_P h_r H_D \quad \textbf{Equation 4}$$

where the effective mass of the pendulum is denoted as *m*, with a value of 0.21 kg. v_{in} represents the initial velocity before the indentation of the indenter, v_{out} denotes the outgoing velocity at the point where the tip detaches from the sample on the initial rebound, A_P is the projected contact area of the indenter. The calculated results are summarized in **Table 1**. For impact at *AF*=5 mN of TaNbHfZr film, the energy contribution to U_{fra} accounts for 17.5% of the kinetic energy difference, which is the primary factor that makes the H_D much smaller than the hardness in quasi-static circumstances, as shown in **Table S1**.

3.2.5 Microstructure characterization by TEM of impact-deformed film

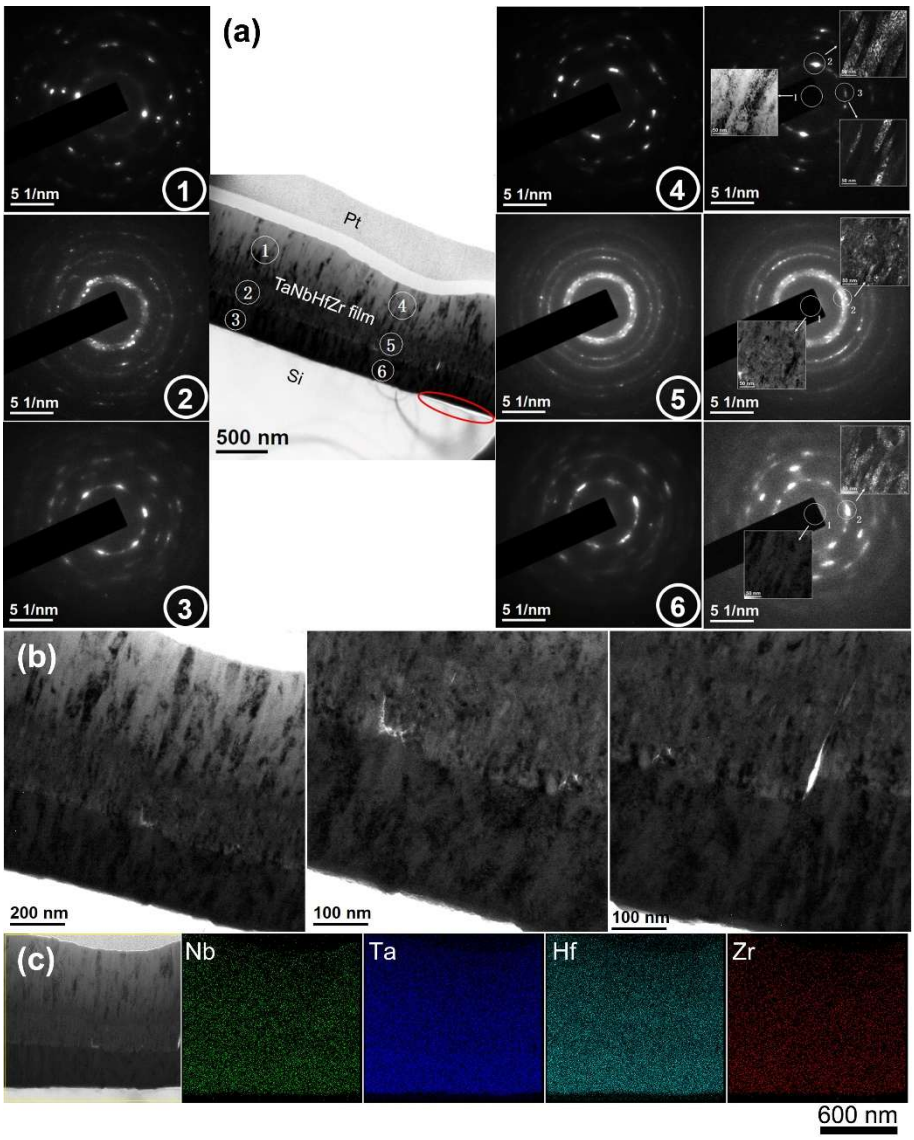

Figure 6 (a) SAED image of the areas located beyond (area ①, ② and ③) and directly below (area ④, ⑤ and ⑥) the indenter, specific spots in the SEAD images indicate the BF (marked "1") and DF (marked "2" and "3" for area ④, marked "2" for area ⑤ and ⑥) images; a delamination gap between the TaNbHfZr film and Si substrate is highlighted by a red circle; **(b)** Cracks in the middle layer near the interface; **(c)** Homogeneous elemental distribution by TEM-EDS mapping of the deformed area throughout the TaNbHfZr film after impact deformation at *AF*=5 mN.

Six sites away from (①, ②, ③) and right below (④, ⑤, ⑥) the indenter are selected to elucidate the microstructural change after impact at 5 mN. As

illustrated in **Figure 6 (a)**, a preferred orientation of the lattice plane is clear and distinct in site ④, which is analogous to that of the as-deposited sample; in site ⑤, dense and continuous pots are connected nearly into separated rings in SAED with visible cracks at the bottom of this zone, enlarged in **Figure 6 (b)**; while in site ⑥, visibly fuzzy and elongated diffraction spots suggest a distorted lattice plane towards various directions, rather than a preferred orientation as seen in the as-deposited film. The grain size of the upper layer ranges of 20 to 50 nm, which is less homogeneous than that of the as-deposited film with a range of 30 to 40 nm; and the grains exhibit a growth direction nearly identical to that of the as-deposited film. The microstructure remains unchanged away from the indenter compared with the as-deposited film. In the deformed area, the extent of deformation is described by the layer thickness change of middle layer: compared with the as-deposited film, the reduction of thickness of the middle layer in nanoindentation at 50 mN was ~9 nm as depicted in **Figure S4**, and ~56 nm in nano-impact at 5 mN. This larger thickness reduction suggests a dynamic response in high-strain-rate nano-impact.

During the impact, the stress distribution is inhomogeneous in the deformed area. Typically, the zone of intense plastic deformation is relatively confined and is limited to a region close to the impact surface [31]. Concurrently, since the absolute value of the tensile stress in the interface center is larger than it for the compressive stress in the surface center [43, 44], the region below the indenter in the film-substrate interface experiences tensile stress, causing the film to bend upwards. This phenomenon can be confirmed from the visible delamination gap shown in **Figure 6 (a)**, marked with red circle. The maximum rebound force, combined with the upward tensile stress and the downward compressive stress induced by the indenter, results in the stress concentration in the middle layer. While at the interface between the middle and bottom layers,

stress cannot be released promptly due to the complex collaborative deformation of the columnar grains in the bottom layer. The dispersion of stress during dynamic deformation is evident, which can be further confirmed by the subsequent FEM simulation.

Large quantities of grain boundaries are present in the middle layer, with equiaxed grains deforming via rotating or grain boundary sliding. This process involves grain boundary dislocations and boundary migration [45] to coordinate and withstand the most severe plastic deformation, strengthening and preventing the entire film from through-thickness crack, fracture or spallation from the substrate. In the bottom layer, the columnar grains become distorted with disordered orientation due to plastic deformation, resulting in fuzzy and elongated spots on the diffraction rings. In contrast, grain distortion occurs in the top layer in quasi-static plastic deformation (**Figure S4**), while it happens in the bottom layer during dynamic deformation. The change in the deformation zone may also be a product of rate-dependent deformation. The EDS mapping result in **Figure 6 (c)** illustrates homogeneous element distribution without segregation or precipitation, notably, this lamination structure maintains its composition even under dynamic impact deformation. Generally, energy loss is equal to the energy stored in the material. Energy-storage mechanisms include crack generation, pore collapse, phase transformations interfacial defects, and frictional processes such as sliding of crack surfaces and dislocations motion [18]. In this study, the TaNbHfZr film loses or stores energy by forming cracks. The amount of the energy can be measured using the fracture energy U_{fra}, as listed in **Table 1**.

3.3 Rate-dependent behavior

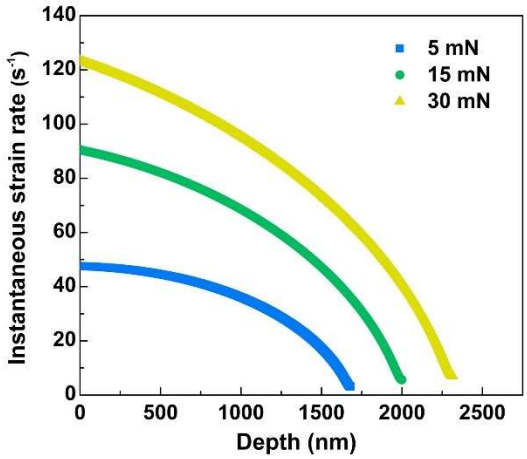

Figure 7. *ISR* of the fitted impact depth-time curve during indentation phase at *AF*=5, 15 and 30 mN.

The *ISR* during indentation can be assumed to be [46]

$$ISR = \frac{v(t)}{h(t)} \qquad \textbf{Equation 5}$$

As *AF* increases, *ISR* in the initial contact of the nano-impact exhibits a corresponding increase, then subsequently decreases over time as shown in **Figure 7**. For the impact at *AF*=5 mN, the initial *ISR* reaches ~50 s^{-1}, which reduces to nearly zero by the end of the indentation process. Pharr has proposed that a larger stress is required to activate the dislocation sources at the early stage of the indentation [47]. For bcc lattice, the motion of screw dislocations often occurs through the thermally assisted formation and migration of kink-pairs [15]. The rate-controlling response is essentially determined by dislocation movement. According to the theory proposed by Hirth & Lothe [48], the nucleation rate of dislocation J_c can be expressed as

$$J_c = nexp\left(-\frac{G}{k_B T}\right) \qquad \textbf{Equation 6}$$

where *n* is a constant of atom sites, K_B is Boltzmann's constant and *T* represents the temperature. The free energy of a dislocation loop, denoted as *G*, generally includes the elastic strain energy of the dislocation, plus

any stacking fault energy, minus the work done by the applied stress [49]. This can be mathematically expressed by

$$G = 2\pi r_c W + \pi {r_c}^2 \gamma - \pi {r_c}^2 b\sigma \qquad \textbf{Equation 7}$$

where r_c is the critical radius of a dislocation loop, γ represents the stacking fault energy, b is the Burgers vector of the dislocation, and σ is the applied stress. It is indicated that an increase in the applied stress σ can effectively reduce G and consequently increase J_c.

During impact, the force of inertia can significantly increase the contact force, resulting in a higher density of dislocation nucleation. At higher *LR*, the film subjected to the indenter experiences higher stress within a unit time, leading to more dislocations near the deformation area. Generally, solute-solution interaction dominates the kinetics of deformation at low flow stress levels, while at higher stress levels, dislocation-dislocation interaction dominates crystal rheology [50]. The deformation mechanism of the nanocrystalline TaNbHfZr film with abundant grain boundaries is dominated by the dislocation-dislocation interaction at higher *AF* with higher strain rate. As the density of dislocation increases at higher strain rates, deformation becomes tougher, providing evidence of the rate-dependent behavior of TaNbHfZr film at dynamic deformation.

3.4 Simulation of stress distribution in the film

FEM simulation was conducted to further confirm the stress distribution within the sandwich-structured TaNbHfZr film. The simulation results indicate that cohesive cracking occurs within the middle layer adjacent to the indentation loading axis. As shown in **Figure 8**, which illustrates the maximum principal stress distribution, it is evident that the topmost indented region experiences significant compressive stress, while the bottom portion undergoes bending tensile stress. The middle layer, situated near the loading axis, is predominantly subject to tensile stress

throughout the layer. This phenomenon is determined by the structure of the three-layer system, and the cracking mechanism can be deduced to be driven by the coupling effect of bending tensile and shear stress. Moreover, the upper surface of the bottom layer is under compression due to the extensive overlying pressure from the middle layer, a situation partly attributable to the higher stiffness (modulus) of the bottom layer compared to the middle one. The simulation results of stress distribution in **Figure 8** well matches and elucidates the indentation-induced damage behavior within the sandwich-layered system with the impact-deformed microstructure in **Figure 6**, where crack events occur when the stress in the middle layer, near the middle-bottom boundary, attains its maximum value.

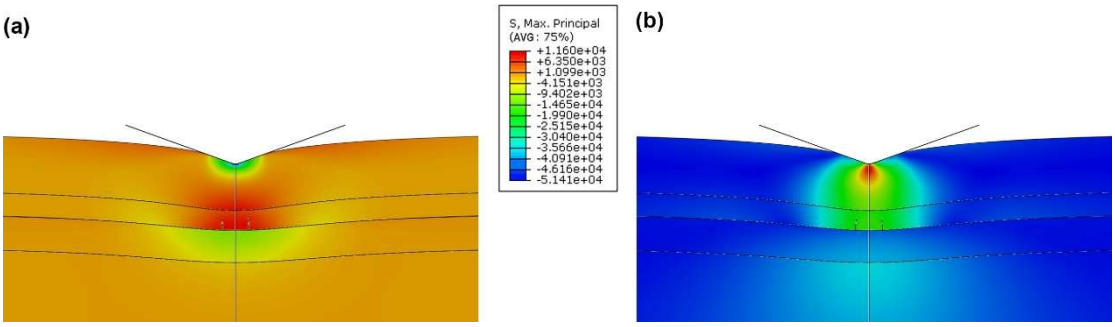

Figure 8 (a) Maximum principal and **(b)** Mises stress distribution of TaNbHfZr film after nanoindentation at 50 mN.

4. Conclusions

The sandwich-structure TaNbHfZr film exhibits rate-dependent behavior during dynamic nano-impact. Cracks are the primary energy-storage mechanism. W_p and U_{fra} increase with strain rates at higher *AF*, and cracks emerge in the middle layer where stress concentrates. The decreased H_D can be explained by the increased energy contribution to fracture at higher strain rates during nano-impact. The equiaxed grains within the middle layer deform through rotation or grain boundary sliding,

thereby accommodating and withstanding the most severe plastic deformation. This process effectively prevents the film from experiencing through-thickness cracking, fracturing, or spallation from the substrate in that the stress was dispersed by interfaces in the sandwich structure.

Examination of the microstructure and the mechanism of dynamic nano-impact of the sandwich-structured TaNbHfZr film provides insights into the overall mechanical performance at nano-scales. This understanding offers valuable evidence and design strategies for materials, particularly refractory high entropy alloy films, when subjected to equivalent high-strain-rate service conditions.

CRediT authorship contribution statement

Baorui Song: Writing – Original draft, Investigation, Conceptualization, Formal analysis, Data curation. **Yanhuai Li**: Conceptualization, Methodology, Writing – review & editing, Validation. **Jiahong Wei**: Investigation. **Dan Qian**: Formal analysis. **Liuquan Yang**: Conceptualization, Visualization. **Zhongxiao Song**: Resources, Software. **Weihua Li**: Project administration, Resources, Supervision, Funding acquisition.

Declaration of Competing Interest

The authors declare that they have no known competing financial interests or personal relationships that could have appeared to influence the work reported in this paper.

Data availability

Data will be made available on request.

Acknowledgements

This work was supported by the Joint Fund of Henan Province Science and Technology R&D Program (225200810090), the Key R&D and

Promotion Project of Henan Province (Science and Technology Research) (232102230039), the Research Start-up Fund of Henan Academy of Sciences (231818023), and the Fundamental Research Fund of Henan Academy of Sciences (230618028).

References

[1] J.W. Yeh, S.K. Chen, S.J. Lin, J.Y. Gan, T.S. Chin, T.T. Shun, C.H. Tsau, S.Y. Chang, Nanostructured high-entropy alloys with multiple principal elements: novel alloy design concepts and outcomes, Adv. Eng. Mater. 6(5) (2004) 299-303.

[2] W. Zhang, P.K. Liaw, Y. Zhang, Science and technology in high-entropy alloys, Sci. China Mater. 61(1) (2018) 2-22.

[3] W.L. Hsu, C.W. Tsai, A.C. Yeh, J.W. Yeh, Clarifying the four core effects of high-entropy materials, Nat. Rev. Chem. 8(6) (2024) 471-485.

[4] E. Ma, X. Wu, Tailoring heterogeneities in high-entropy alloys to promote strength-ductility synergy, Nat. Commun. 10(1) (2019) 5623.

[5] O.N. Senkov, G.B. Wilks, D.B. Miracle, C.P. Chuang, P.K. Liaw, Refractory high-entropy alloys, Intermetallics 18(9) (2010) 1758-1765.

[6] W. Xiong, A.X.Y. Guo, S. Zhan, C.T. Liu, S.C. Cao, Refractory high-entropy alloys: A focused review of preparation methods and properties, J. Mater. Sci. Technol. 142 (2023) 196-215.

[7] Y.D. Wu, Y.H. Cai, X.H. Chen, T. Wang, J.J. Si, L. Wang, Y.D. Wang, X.D. Hui, Phase composition and solid solution strengthening effect in TiZrNbMoV high-entropy alloys, Mater. Des. 83 (2015) 651-660.

[8] C.C. Juan, K.K. Tseng, W.L. Hsu, M.H. Tsai, C.W. Tsai, C.M. Lin, S.K. Chen, S.J. Lin, J.W. Yeh, Solution strengthening of ductile refractory HfMo x NbTaTiZr high-entropy alloys, Mater. Lett. 175 (2016) 284-287.

[9] X.B. Feng, J.Y. Zhang, Y.Q. Wang, Z.Q. Hou, K. Wu, G. Liu, J. Sun, Size effects on the mechanical properties of nanocrystalline NbMoTaW refractory high entropy alloy thin films, Int. J. Plasticity 95 (2017) 264-277.

[10] A.A. El-Aty, Y. Xu, S.-H. Zhang, S. Ha, Y. Ma, D. Chen, Impact of high strain rate deformation on the mechanical behavior, fracture mechanisms and anisotropic response of 2060 Al-Cu-Li alloy, J. Adv. Res. 18 (2019) 19-37.

[11] Y. Tang, D.Y. Li, Dynamic response of high-entropy alloys to ballistic impact, Sci. Adv. 8 (2022) eabp9096.

[12] M. Rueda-Ruiz, B.D. Beake, J.M. Molina-Aldareguia, New instrumentation and analysis methodology for nano-impact testing, Mater. Des. 192 (2020) 108715.

[13] G.I. G.T., F. P.S., Influence of peak pressure and pulse duration on substructure development and threshold stress measurements in shock loaded copperL, Impact Loading and Dynamic Behavior of Materials 2, DCM Informationsgesellschaft Verlag (1988) 541-548.

[14] E. Hirscha, J. Plesekb, A theoretical analysis of experimental results of shock wave loading of OFE copper relating the observed internal structure to the deformation mechanism, Int. J. Impact Eng. 32(8) (2006) 1339-1356.
[15] A. Ghafarollahi, W.A. Curtin, Theory of kink migration in dilute BCC alloys, Acta Mater. 215 (2021) 117078.
[16] S. NEMAT-NASSER, J.B. ISAACS, M. LIU, Microstructure of high-strain, high-strain-rate deformed Tantalum, Acta Mater. 46(4) (1998) 1307-1325.
[17] G. Dirras, H. Couque, L. Lilensten, A. Heczel, D. Tingaud, J.-P. Couzinié, L. Perrière, J. Gubicza, I. Guillot, Mechanical behavior and microstructure of Ti20Hf20Zr20Ta20Nb20 high-entropy alloy loaded under quasi-static and dynamic compression conditions, Mater. Charact. 111 (2016) 106-113.
[18] R.W. KLOPP, R.J. CLIFTON, T.G. SHAWKI, Pressure-shear impact and the dynamic viscoplastic response of metals, Mech. Mater. 4 (1985) 375-385.
[19] Q. Wei, T. Jiao, K.T. Ramesh, E.Ma, Nano-structured vanadium: processing and mechanical properties under quasi-static and dynamic compression, Scripta Mater. 50(3) (2004) 359-364.
[20] S. Wei, E.S. Park, S.J. Kim, J. Kang, Y. Zhang, Y. Zhang, T. Furuhara, E.S. Park, C.C. Tasan, Natural-mixing guided design of refractory high-entropy alloys with as-cast tensile ductility, Nat. Mater. 19(11) (2020) 1175-1181.
[21] Y.F. Zhao, Y.Q. Wang, K. Wu, J.Y. Zhang, G.Liu, J. Sun, Unique mechanical properties of Cu/(NbMoTaW) nanolaminates, Scripta Mater. 154 (2018) 154-158.
[22] J.M. Wheeler, J. Dean, T.W. Clyne, Nano-impact indentation for high strain rate testing: The influence of rebound impacts, Extreme Mech. Lett. 26 (2019) 35-39.
[23] M.R. Marulli, A. Valverde-González, A. Quintanas-Corominas, M. Paggi, J. Reinoso, A combined phase-field and cohesive zone model approach for crack propagation in layered structures made of nonlinear rubber-like materials, Comput. Method. in Appl. M. 395 (2022).
[24] S. Maiti, W. Steurer, Structural-disorder and its effect on mechanical properties in single-phase TaNbHfZr high-entropy alloy, Acta Mater. 106 (2016) 87-97.
[25] B. Song, Y. Li, Z. Cong, Y. Li, Z. Song, J. Chen, Effects of deposition temperature on the nanomechanical properties of refractory high entropy TaNbHfZr films, J. Alloy. Compd. 797 (2019) 1025-1030.
[26] I. Petrov, P. B. Barna, L. Hultman, J.E. Greene, Microstructural evolution during film growth, J. Vac. Sci. Technol. A 21(5) (2003) S117-S128.
[27] B. Sboui, D. Rodney, P.-A. Geslin, Elastic modelling of lattice distortions in concentrated random alloys, Acta Mater. 257 (2023) 119117.
[28] W.L. Wang, L. Hu, S.J. Yang, A. Wang, L. Wang, B. Wei, Liquid supercoolability and synthesis kinetics of quinary refractory high-entropy alloy, Sci. Rep.-UK 6 (2016) 37191.
[29] A. Zafari, K. Xia, Laser powder bed fusion of ultrahigh strength Fe-Cu alloys using elemental powders, Addit. Manuf. 47 (2021).

[30] M.J. Bermingham, D.H. StJohn, J. Krynen, S. Tedman-Jones, M.S. Dargusch, Promoting the columnar to equiaxed transition and grain refinement of titanium alloys during additive manufacturing, Acta Mater. 168 (2019) 261-274.
[31] X. Shi, J. Chen, B.D. Beake, T.W. Liskiewicz, Z. Wang, Dynamic contact behavior of graphite-like carbon films on ductile substrate under nano/micro-scale impact, Surf. Coat. Tech. 422 (2021) 127515.
[32] K.M. Conway, C. Kunka, B.C. White, G.J. Pataky, B.L. Boyce, Increasing fracture toughness via architected porosity, Mater. Des. 205 (2021) 109696.
[33] K. Komvopoulos, Finite element analysis of a layered elastic solid in normal contact with a rigid surface, J. Tribol.-T. ASME 110 (1988) 477-485.
[34] P. Klose, V. Roddatis, A. Pundt, Tuning the stress state in Nb-thin films by lateral size confinement, Acta Mater. 222 (2022) 117454.
[35] J. Chen, X. Shi, B.D. Beake, X. Guo, Z. Wang, Y. Zhang, X. Zhang, S.R. Goodes, An investigation into the dynamic indentation response of metallic materials, J. Mater. Sci. 51(18) (2016) 8310-8322.
[36] D. Tabor, The Hardness of Metals, Clarendon Press, Oxford, 1951.
[37] N.M. Jennett, J. Nunn, High resolution measurement of dynamic (nano) indentation impact energy: a step towards the determination of indentation fracture resistance, Philos. Mag. 91(7-9) (2011) 1200-1220.
[38] E.W. Andrews, A.E. Giannakopoulos, E. Plisson, S. Suresh, Analysis of the impact of a sharp indenter, Int. J. Solids Struct. 39 (2002) 281-295.
[39] G. Constantinides, C.A. Tweedie, N. Savva, J.F. Smith, K.J.V. Vliet, Quantitative Impact Testing of Energy Dissipation at Surfaces, Exp. Mech. 49(4) (2009) 511-522.
[40] R. Sahaa, Z. Xue, Y. Huang, W. Nix, Indentation of a soft metal film on a hard substrate: strain gradient hardening effects, J. Mech. Phys. Solids 49 (2001) 1997-2014.
[41] K. Wang, N.R. Tao, G. Liu, J.Lu, K.Lu, Plastic strain-induced grain refinement at the nanometer scale in copper, Acta Mater. 54(19) (2006) 5281-5291.
[42] A.A. Elmustafa, D.S. Stone, Indentation size effect in polycrystalline F.C.C. metals, Acta Mater. 50 (2002) 3641-3650.
[43] M. Stefenelli, R. Daniel, W. Ecker, D. Kiener, J. Todt, A. Zeilinger, C. Mitterer, M. Burghammer, J. Keckes, X-ray nanodiffraction reveals stress distribution across an indented multilayered CrN–Cr thin film, Acta Mater. 85 (2015) 24-31.
[44] Y. IWAHASHI, Z. HORITA, M. NEMOTO, T.G. LANGDON, The process of grain refinement in equal-channel angular pressing, Acta Mater. 46(9) (1998) 3317-3331.
[45] G.S. Rohrer, I. Chesser, A.R. Krause, S.K. Naghibzadeh, Z. Xu, K. Dayal, E.A. Holm, Grain Boundary Migration in Polycrystals, Annu. Rev. Mater. Res. 53(1) (2023) 347-369.
[46] B.N. LUCAS, W.C. OLIVER, Indentation power-law creep of high-purity Indium, Metall. Mater. Trans. A 30A 601-610.
[47] G.M. Pharr, E.G. Herbert, Y. Gao, The Indentation Size Effect: A Critical Examination of Experimental Observations and Mechanistic Interpretations,

Annu. Rev. Mater. Res. 40(1) (2010) 271-292.
[48] P.M. Anderson, J.P. Hirth, J. Lothe, Theory of Dislocations, Cambridge University Press, 2017.
[49] A.B.MANN, P.C.SEARSON, J.B.PETHICA, T.P.WEIHS, The relationship between near-surface mechanical properties, loading rate and surface chemistry, Mat. Res. Soc. Symp. Proc. 505 (1998) 307-318.
[50] A.A. Elmustafa, D.S. Stone, Nanoindentation and the indentation size effect: kinetics of deformation and strain gradient plasticity, J. Mech. Phys. Solids 51 (2003) 357-381.